

RESEARCH ARTICLE

Bionic surface diode for droplet steering

Xiaolong Yang^{1,2} | Biao Qi¹  | Yao Lu³  | Wang Zhang⁴ | Xiaolei Wang¹¹College of Mechanical and Electrical Engineering, Nanjing University of Aeronautics and Astronautics, Nanjing, China²Jiangsu Key Laboratory of Precision and Micro-Manufacturing Technology, Nanjing University of Aeronautics and Astronautics, Nanjing, China³Department of Chemistry, School of Physical and Chemical Sciences, Queen Mary University of London, London, UK⁴Engineering Product Development, Singapore University of Technology and Design, Singapore, Singapore

Correspondence

Xiaolei Wang, College of Mechanical and Electrical Engineering, Nanjing University of Aeronautics and Astronautics, Nanjing 210016, China.

Email: wxl@nuaa.edu.cn

Funding information

National Natural Science Foundation of China, Grant/Award Number: 51905267; Natural Science Foundation of Jiangsu Province, Grant/Award Number: BK20190411; China Postdoctoral Science Foundation, Grant/Award Numbers: 2020TQ0148, 2021M700072; Fundamental Research Funds for the Central Universities, Grant/Award Number: NT2020011; Opening foundation of Aero-engine Thermal Environment and Structure Key Laboratory of Ministry of Industry and Information Technology of China, Grant/Award Number: CEPE2020008

Abstract

Control of droplet sliding and its interfacial behavior such as sliding resistance and friction have important applications in microfluidic and energy-related fields. Nature provides many examples of interface-driven droplet sliding control; yet, to date, the continuous governing of the multiphase process and precise steering of droplet sliding remain challenging. Here, directional-dependent ultraslippery patterned surfaces with significant droplet sliding anisotropy were created by coordinating the heterogeneous wettability of the back of the desert beetle, directional-dependent architecture of the butterfly wing, and ultraslippery configuration of the *Nepenthes alata*. Analysis of the sliding resistance on typical ultraslippery patterned surfaces reveals that the directional-dependent triple phase line (TPL) immigration on the ultraslippery patterns dominates the strong sliding anisotropy, which can be modeled using the classic Fumidge equation. In particular, the sliding anisotropy for the semicircular ultraslippery patterned surface shows threefold higher than that of natural butterfly wings due to the most significant difference in TPL immigration in two opposite directions, which enables the simultaneous handling of multiple droplets without mass loss and steering of droplet sliding/friction. This work may transform the design space for the control of multiphase interface motion and the development of new lab-on-a-chip and droplet-based microsystems.

INTRODUCTION

Droplet manipulations such as storage, transfer, and mixing have always been crucial subjects to researchers due to their potential applications in microfluidic,^{1–7} tribology,^{8,9} and energy harvest.^{10–14} Lotus leaf-inspired superhydrophobic surfaces (with water contact angle >150°) are considered to be an ideal platform for manipulating the droplets because their excellent water repellency tends to suspend the bead-like

droplet, which enables simple and convenient operations, for example, transfer and coalescence. Homogeneous superhydrophobic surfaces exhibit isotropic droplet adhesion,^{15,16} thus sophisticated manipulations that necessitate droplet transport on the designed path are restricted. Coordination between superhydrophobicity and external stimuli, such as light,^{17,18} electricity,^{19,20} pH,²¹ temperature,²² magnetism,²³ and so forth, is an advisable strategy to achieve such exquisite functions. However, stimulus-responsive superhydrophobic surfaces are not

Xiaolong Yang and Biao Qi contributed equally to this study.

This is an open access article under the terms of the Creative Commons Attribution License, which permits use, distribution and reproduction in any medium, provided the original work is properly cited.

© 2023 The Authors. *Droplet* published by Jilin University and John Wiley & Sons Australia, Ltd.

suitable for mild biomedical applications and the engineering aspects that the stimuli cannot access. Alternately, sliding anisotropy enlightened by the Araucaria leaf,⁶ the rice leaf,²⁴ and butterfly wings^{25,26} allows for precise control of droplet motion due to the directional-dependent sliding resistance that can guide the droplet moving in desired directions. Several exquisite studies^{27–29} were reported to formulate the design strategy of directional-dependent structures for fantastic liquid/droplet steering. In addition, the creation of the sliding anisotropy is readily feasible by patching wettability contrast patterns with high adhesion on roll-off superhydrophobic substrates,^{30–36} yet droplets tend to be detained on the patterns, resulting in the loss of mass and the increased possibility of cross-contamination.

A slippery lubricant-infused porous surface (SLIPS) inspired by *Nepenthes alata* plants has been widely applied for droplet motion control due to its intrinsic properties of ultralow contact angle hysteresis, self-healing, pressure stability, and being immiscible with manipulated droplets.^{37–44} The SLIPS patterns show strong affinity toward the deposited droplet but exhibit ultralow sliding resistance without absorption due to the immiscible droplet–lubricant interface, which is similar to the hydrophilic patterns from the aspect of stress condition but has no risk of mass loss.^{45–47} As a result, it is possible to patch SLIPS patterns on the roll-off superhydrophobic background to precisely control the droplet motion. A few notable studies succeeded in simultaneously transferring multiple droplets by taking the advantage of anisotropic droplet sliding on SLIPS patterns.^{48,49} Nevertheless, the fundamental impact of SLIPS pattern geometry on the sliding resistance is unclear. In addition, continuous governing of droplet movement instead of controlling a droplet over an individual pattern, for example, steering of droplet friction engenders more cutting-edge applications, yet remains challenging.

In this work, we report multi-bioinspired SLIPS-patterned superamphiphobic surfaces by coordinating the heterogeneous wettability of the back of the desert beetle, directional-dependent architecture of the butterfly wing, and ultraslippery configuration of the *N. alata*. The droplet sliding resistance on this multi-bioinspired surface can be well controlled by the geometry, size, and arrangement of the SLIPS patterns, which follows the classic dragging resistance model (Furmidge equation). The maximum obtained sliding anisotropy obtained by the surface shows threefold higher than that of natural butterfly wings, which enables the handling of multiple droplets without mass loss simultaneously and precise steering of droplet friction by carefully architecting the patterns. We envision the functional architected surface as a complementary platform to conventional surface engineering, enabling applications such as droplet-based microfluidic, tribology, and energy-harvesting devices.

RESULTS AND DISCUSSION

The back of the desert beetle is a typical heterogeneous wettability surface, consisting of a hydrophobic background and hydrophilic patches. The hydrophilic patches serve as a high adhesion trap

that can catch the surrounding mist in the desert.⁵⁰ However, the hydrophilic patches (typically with the directional-independent circular shape) on the back of the desert beetle show isotropic adhesion, which is not intended for sophisticated droplet motion control.⁵¹ Butterfly wings with directional-dependent shapes and arrangement of overlapping scales exhibit controllable anisotropic adhesion enabling directional droplet sliding (Figure 1a).²⁵ Integrated with the heterogeneous wettability, the flexible control over adhesion and sliding direction further extends the droplet manipulations and ensures diverse applications.^{12,34,52} Moreover, when we combine the high mobility configuration of *N. alata* with the above-mentioned two distinct wettability scenarios, multi-bioinspired SLIPS-patterned surfaces that allow for directional droplet sliding and precise steering of droplet friction were created (Figure 1a,b). A simple method involving electrochemical etching, chemical vapor deposition of a fluorinated silane, laser ablation, and lubricant infusing was proposed for the scaled-up fabrication in real-world applications (Supporting Information: Figure S1).

The electrochemical etching combined with boiling water soaking creates concave microstructures covered with dense nanovillus, as shown in the scanning electron microscopy (SEM) images (Figure 1c and Supporting Information: Figure S2). These hierarchical micro/nanostructures were crucial for superamphiphobicity.^{53,54} After chemical vapor deposition of fluorinated silane,⁵⁵ the elements of C and F were detected, which represented that low surface energy components were successfully assembled on the surface, as shown in the energy-dispersive spectroscopy (EDS) (Figure 1d). Both DI water and hexadecane droplets dispensed on the prepared superamphiphobic surface manifested contact angles larger than 150° and sliding angles less than 10°, displaying excellent static and dynamic superamphiphobicity (Supporting Information: Movie S1). Laser ablation induces phase explosion, rapid evaporation, melting, and resolidification,^{56,57} thus enabling site-selectively removal of micro/nanostructures and the overlaid low surface energy layer. The EDS spectra of the laser-ablated region show that the element of F was substantially reduced after laser ablation. The tailoring of the structure and chemical component in the laser-ablated region resulted in a rapid wettability transition from superamphiphobicity to superhydrophilicity with contact angles of ~0°. As a result, the superhydrophilic patterns with complex two-dimensional geometries can be readily created on the superamphiphobic background via scanning path control of the laser ablation. After dipping the patterned surface in the lauric acid-modified hexadecane, the superhydrophilic patterns were then rendered superhydrophobic due to a self-assembled monolayer formed by spontaneous absorption of lauric acid^{48,58} and, meanwhile, the patterned regions were infused with hexadecane, which was used as a lubricant, to reach a stable ultraslippery state.³⁹

Insight into triple phase line (TPL) pinning and immigration of a deposited droplet on SLIPS patterns are crucial for sliding control because they determine the droplet-pattern interface and the corresponding sliding resistance. To validate the dependence of SLIPS pattern geometries on the sliding resistance, three typical directional-dependent SLIPS patterns evolved from the architecture

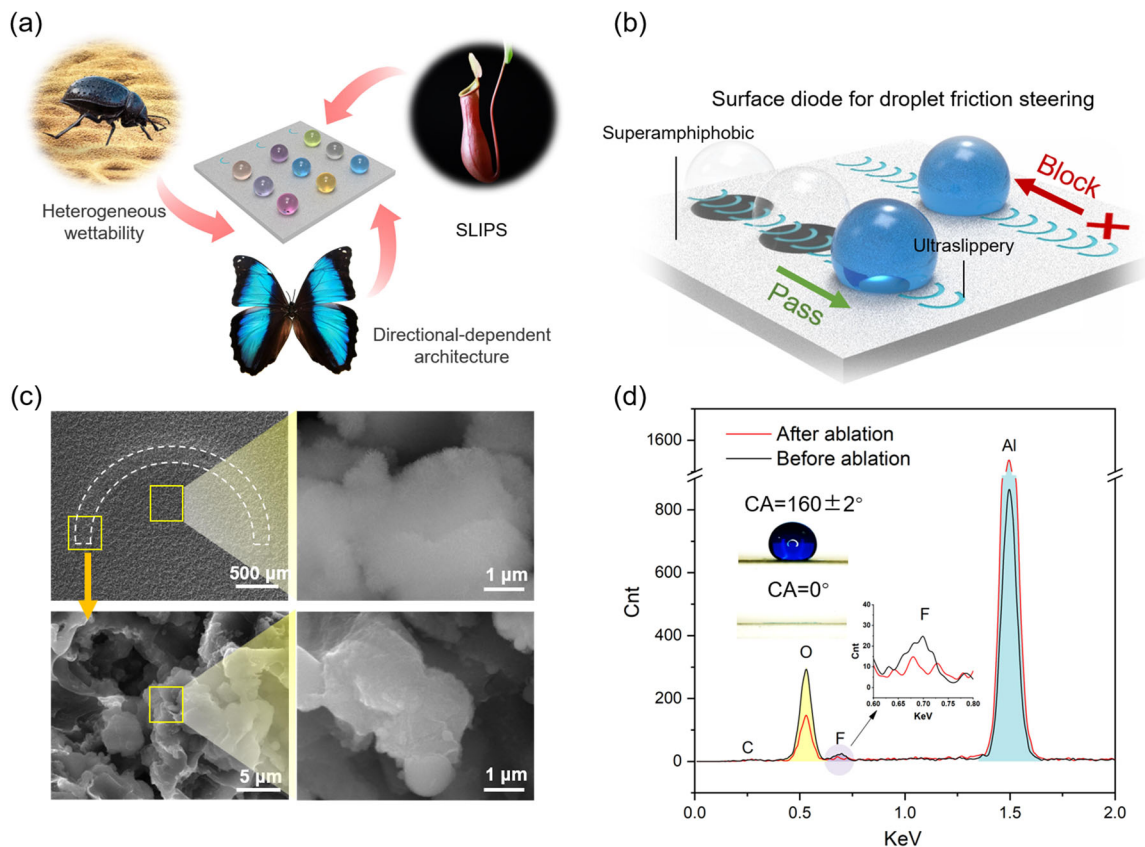


FIGURE 1 Construction of multi-bioinspired slippery lubricant-infused porous surfaces patterned surfaces: (a) schematic of surface construction by coordinating heterogeneous wettability of the back of the desert beetle, directional architecture of the butterfly wing, and ultraslippery configuration of the *Nepenthes alata*; (b) schematic of steering droplet friction on the multi-bioinspired surface; (c) scanning electron microscopy images; and (d) energy-dispersive spectroscopy spectra of the background and the pattern region before lubricant infusing the pattern.

of butterfly wings were designed. Those include the arrow-shaped (Figure 2a), horn-shaped (Figure 2d), and semicircular SLIPS patterns (Figure 2g). Among them, the horn-shaped and semicircular SLIPS patterns can be treated as derivations of the arrow-shaped ones by endowing the edge line with positive and negative curvatures, respectively. The arrow-shaped SLIPS patterns mainly involve three parameters: line width (W), included angle (β), and line length (L), while both the horn-shaped and semicircular SLIPS patterns are described by line width (W) and curvature radius (R). To quantitatively characterize the directional sliding on the directional-dependent SLIPS patterns, the sliding angles in the outward (D_{out}) and inward direction (D_{in}) of the patterns were measured (Supporting Information: Figure S3). In the experiment, 15 μ l of DI water droplets was used to ensure that the pattern was fully covered by the droplet footprint. The sliding resistance F_{re} was obtained according to force equilibrium:

$$F_{re} = m \times g \times \sin \alpha, \quad (1)$$

where m is the mass of the droplet, g is the gravitational acceleration, and α is the measured sliding angle. According to the Furmidge equation, the resistance of a droplet sliding off patterned surface is proportional to the droplet-pattern interfacial width

W_{dro} perpendicular to the sliding direction, given by the following formula⁵⁹⁻⁶¹

$$F_{re} = \gamma \times W_{dro} (\cos \theta_R - \cos \theta_A), \quad (2)$$

where γ is the surface tension of water, θ_A is the advancing contact angle on the superamphiphobic background, and θ_R represents the receding contact angle on the SLIPS pattern. For a given liquid, γ is constant, and both the θ_A and θ_R are also fixed for a specific wettability scenario. Thus, W_{dro} becomes the principal parameter that dominates the sliding resistance.

Sliding resistances of droplets on arrow-shaped (Figure 2b,c), horn-shaped (Figure 2e,f), and semicircular (Figure 2h,i) SLIPS patterns in D_{out} and D_{in} directions were measured. The line width W determines the droplet-pattern interfacial width W_{dro} and the sliding resistance in a most simple way. The W_{dro} increases with the line width W , thus resulting in enlarged sliding resistance for all the three SLIPS patterns. An interesting phenomenon was that sliding resistance in D_{in} was much higher than that in D_{out} , showing excellent sliding anisotropy (defined as the difference between sliding resistance in the two opposite directions) for all these demonstrated patterns (Figure 2j). The directional-dependent sliding was ascribed to the pinning and immigration of TPL.³⁴ When the droplet slid in the

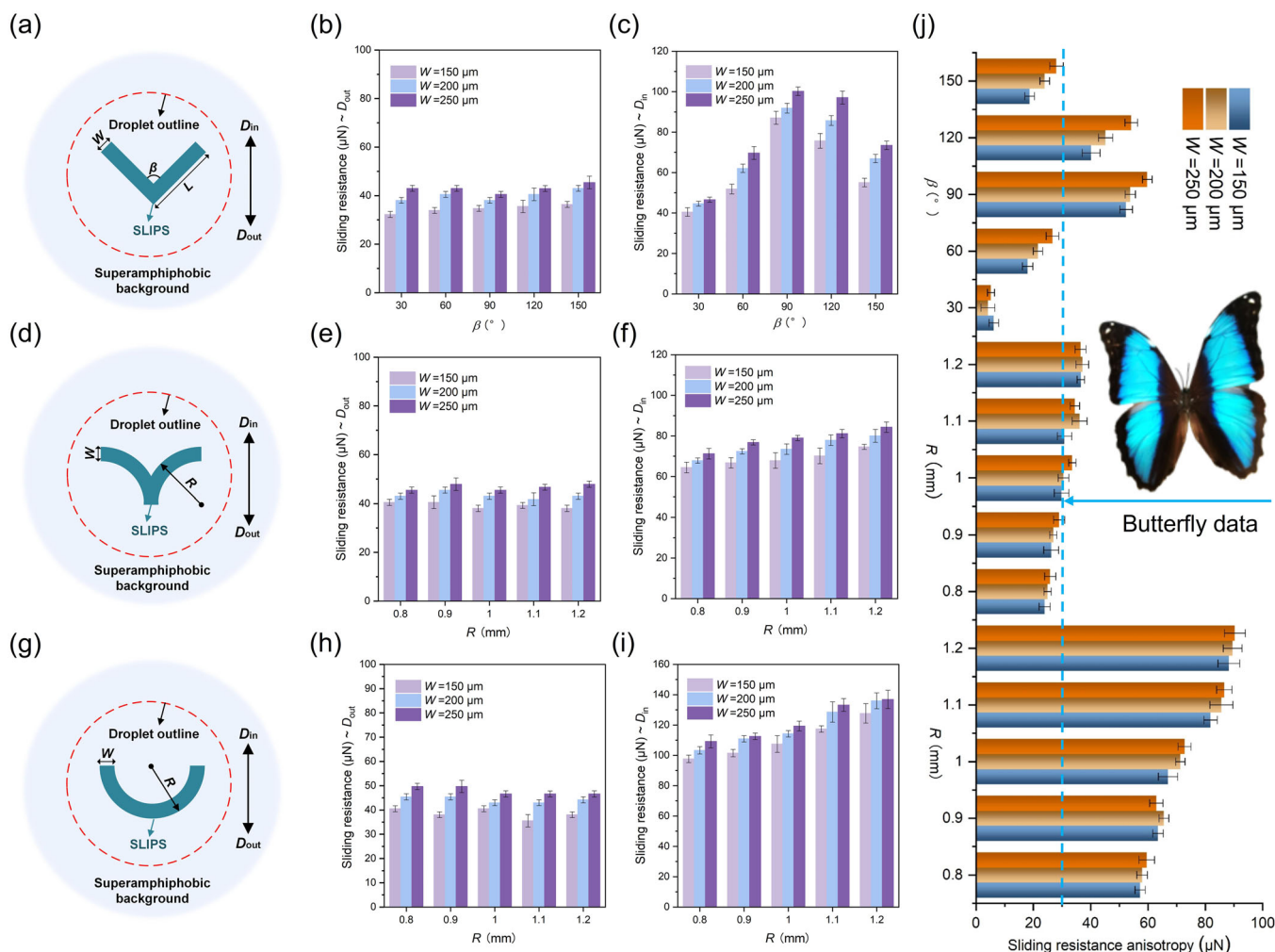


FIGURE 2 Droplet sliding control on slippery lubricant-infused porous surface (SLIPS)-patterned surfaces: schematic of (a) arrow-shaped, (d) horn-shaped, and (g) semicircular SLIPS patterns; sliding resistance in D_{out} direction on (b) arrow-shaped, (e) horn-shaped, and (h) semicircular SLIPS patterns; sliding resistance of droplets in D_{in} direction on (c) arrow-shaped, (f) horn-shaped, and (i) semicircular SLIPS patterns; and (j) sliding resistance anisotropy versus main parameters of different SLIPS patterns (from top to bottom corresponds to arrow-shaped, horn-shaped, and semicircular SLIPS patterns, respectively). The volume of the droplet used in the experiment was $15 \mu\text{l}$.

outward direction (D_{out}), the TPL immigrated from the tail end of the SLIPS pattern to the middle due to the intrinsic high mobility property of SLIPS and the W_{dro} was reduced to the middle region of the pattern (upper panel in Figure 3a), thereby contributing to a smaller outward sliding resistance (Figure 2b). On the contrary, regarding the droplet sliding in the inward direction (D_{in}), the TPL was likely to be pinned at the tail end with only slight deflection due to the inconspicuous mismatching of TPL to the pattern profile at the tail region for arrow-shaped SLIPS patterns (lower panel in Figure 3a). Therefore, the W_{dro} almost equaled but was slightly smaller than the tail gap distance of the pattern; thus, a much higher inward sliding resistance and obvious sliding anisotropy were obtained (Figure 2c,j). For a fixed included angle of the arrow-shaped SLIPS pattern, the inward sliding resistance and the resultant sliding anisotropy increased with the line length L because it was proportional to the tail gap distance and the W_{dro} in the inward direction (Supporting Information: Figure S4), while the outward sliding resistance was not affected.

However, an enlarged included angle ($>90^\circ$) of the arrow-shaped pattern exacerbated the mismatching of the TPL to the pattern profile in inward (D_{in}) sliding, which resulted in the TPL immigration to the middle region of the pattern,⁶² similar to that sliding in the outward direction (D_{out}). As a result, W_{dro} was downsized, and both the inward sliding resistance and sliding anisotropy were weakened, considering that the outward sliding resistance remained almost unchanged (Figure 2b). A typical example is that inward sliding on a pattern with an included angle larger than 180° would be transited into the condition of low-resistance outward sliding. Therefore, regarding the included angle, a maximum inward sliding resistance and sliding anisotropy existed and was located at 90° (Figure 2c,j).

The sliding anisotropy was also evidenced on the horn-shaped SLIPS patterns (Figure 2d-f). The TPL immigration-induced easy roll-off of droplets in the outward direction (D_{out}) was the same as other patterns (Figure 2e). The mismatching of the TPL to the pattern profile in inward (D_{in}) sliding was further promoted because the

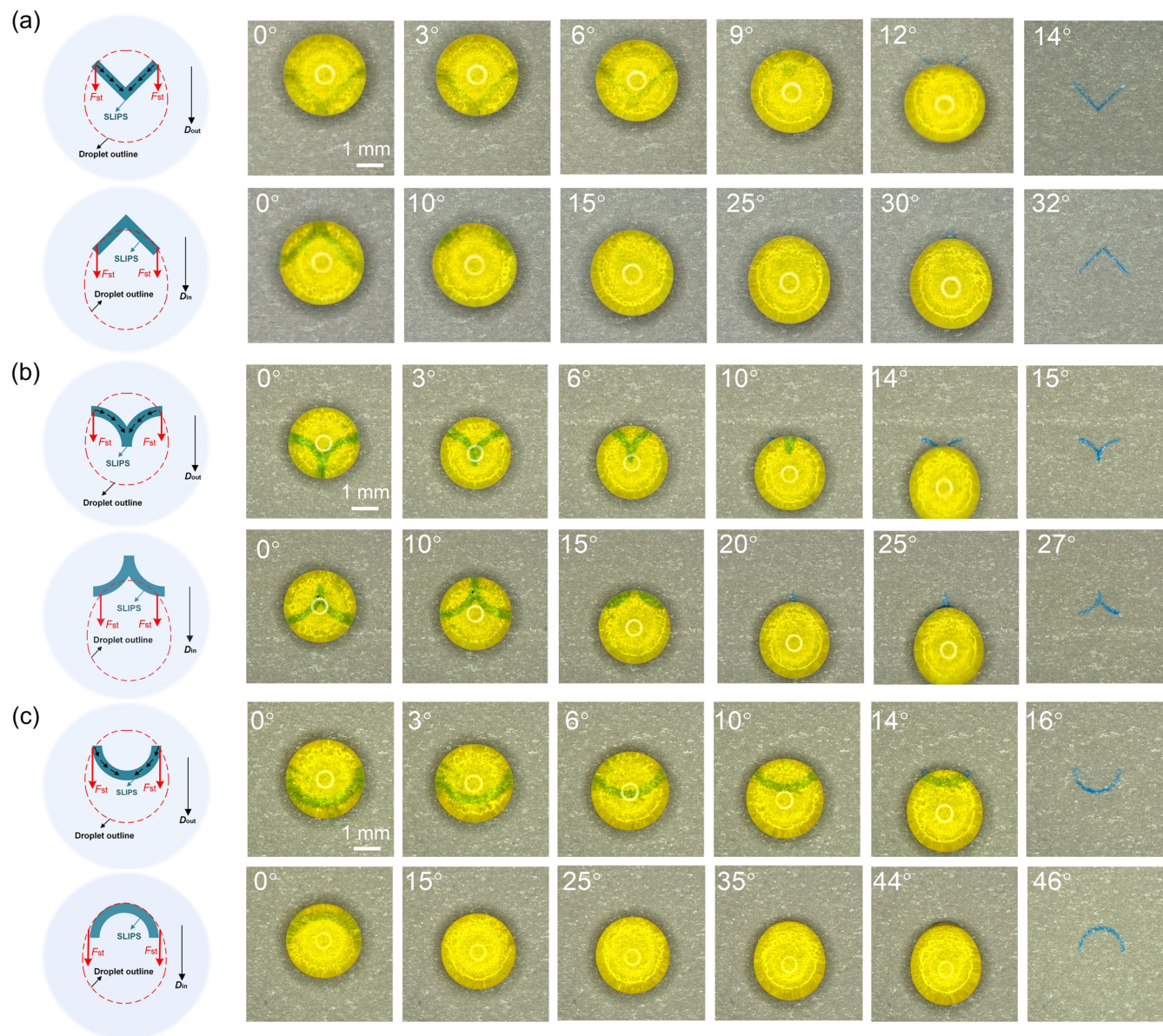


FIGURE 3 Schematic and bird-eye view optical images of DI water droplets sliding off the slippery lubricant-infused porous surface (SLIPS) patterns: droplets sliding off the (a) arrow-shaped, (b) horn-shaped, and (c) semicircular SLIPS patterns in outward (D_{out} , upper panels) and inward (D_{in} , lower panels) directions. F_{st} is defined as the surface tension of the droplet. The droplet with the volume of $15 \mu\text{l}$ was dyed yellow for better visualization. The measured surface tensions of DI water and dyed water are 73.06 and 72.84 mN/m , respectively, at room temperature (20°C), which indicates that the dye almost has no effect on the surface tension of the liquid.

curvature of the pattern profile was completely opposite to the TPL. Therefore, the sliding resistance in the inward direction (D_{in}) and the sliding anisotropy were weakened (Figures 2f and 3b), compared with the arrow-shaped SLIPS patterns.

The most significant sliding anisotropy was observed on the semicircular SLIPS pattern (Figures 2g-j and 3c). The sliding resistance in the outward direction (D_{out}) was maintained at a low value of $46.6 \mu\text{N}$. Regarding the inward (D_{in}) directions, the TPL immigration can be neglected due to the perfect matching of the curvature of the pattern profile to the curvature of the TPL (Figure 3c). The W_{dro} was thereby maximized to equal the tail gap distance. The maximum inward sliding

resistance of $136.9 \mu\text{N}$ and the sliding anisotropy of as high as $90.3 \mu\text{N}$ were obtained. It was notable that the sliding anisotropy was threefold higher than the averaged measurements ($29.9 \mu\text{N}$) on 29 species of butterfly wings.⁶³ Meanwhile, the sliding resistance on the homogeneous SLIPS without any patterns is around $5.13 \mu\text{N}$ in all directions, displaying isotropic sliding (Supporting Information: Figure S5). This further verified that the directional-dependent SLIPS patterns have an effective capability of steering droplet sliding. In addition, we tested the sliding anisotropy of droplets with a different volume ($5 \mu\text{l}$) and the results indicated that the patterns functioned well for droplets with varied volumes (Supporting Information: Figure S6).

Prediction of the droplet sliding resistance is essential for designing reliable functional surfaces for sophisticated droplet manipulations,⁶⁴ such as droplet capturing, transferring, mixing, and so forth. In this work, we applied the Furmidge equation to calculate the resistance of droplets sliding off the SLIPS patterns. The Furmidge equation formulates the linear relationship between the sliding resistance and the droplet-pattern interfacial width W_{dro} that is perpendicular to the sliding (Equation 2). The most important task is to determine the W_{dro} because the other input parameters are constant for a given liquid and surface wettability. Here, the W_{dro} for semicircular SLIPS patterns can be obtained by directly measuring the dimensions of the pattern due to the perfect matching of the curvature of the SLIPS pattern to the TPL. For example, W_{dro} in the inward direction is the tail distance and outward W_{dro} is the width of the solid area at the middle region (Figure 4c). However, regarding the arrow-shaped and horn-shaped SLIPS patterns, the W_{dro} could not be measured directly, and it was acquired by dragging the droplet toward corresponding directions and measuring the interfacial width at sliding-off moment (Figure 4a-c). By integrating the W_{dro} into Equation (2), the model-predicted sliding resistances were plotted in Figure 4d-f and found to be in good matching with the experimentally measured data. According to the above discussion, the semicircular SLIPS pattern showed the most significant sliding

anisotropy, which can be precisely predicted by the designed dimension of the pattern.

It is thus clear that the semicircular SLIPS pattern has priority when selected for creating functional surfaces to control the droplet sliding and develop advanced droplet manipulation platforms. For example, the capturing and releasing of microliter-sized droplets are the basis of molecular detection such as mass spectrometry and high-performance liquid chromatography.^{65,66} It is essential to avoid mass loss of the droplet during the manipulation. Many methods that involve in situ control of surface wettability,⁶⁷ architecture,⁶⁸ and surface charge⁶⁹ for droplet manipulation without mass loss have been reported in the past few years. These are promising approaches for handling single droplets, but the operation of multiple droplets simultaneously remains challenging. We here applied two face-to-face semicircular SLIPS-patterned surfaces for this purpose. By taking the advantage of the significant sliding anisotropy of the surface, only vertical and horizontal movements of the upper surface were needed for operating an array of droplets (Figure 5a,b). For example, moving the upper surface in a large sliding resistance direction (D_{in}) at the contacting state can capture the droplet array from the lower surface (Figure 5c). On the contrary, moving the upper surface in a small sliding resistance direction (D_{out}) is the trigger for releasing the droplet array (Figure 5d; Supporting Information: Movie S2). This simple process can

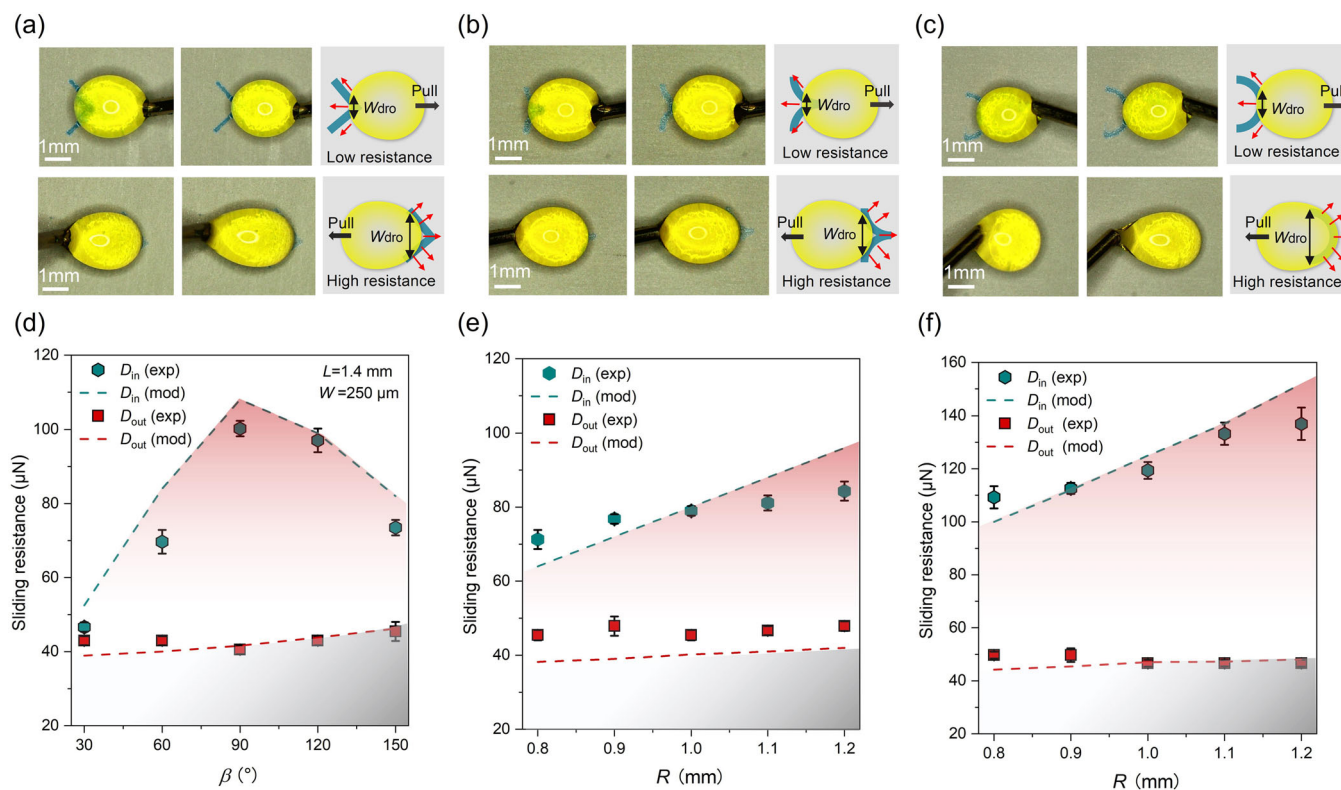


FIGURE 4 Prediction of sliding resistance: bird-eye view optical images of dragging a dyed DI water droplet off the (a) arrow-shaped, (b) horn-shaped, and (c) semicircular slippery lubricant-infused porous surface (SLIPS) patterns in D_{out} and D_{in} directions for measuring the W_{dro} ; experimentally measured and model predicted sliding resistance on the (d) arrow-shaped, (e) horn-shaped, and (f) semicircular SLIPS patterns in D_{out} and D_{in} directions. The droplet volume used for the measurement of sliding resistance was 15 μl . Error bars of some sliding resistance data in D_{out} are too small to be visible in (d-f).

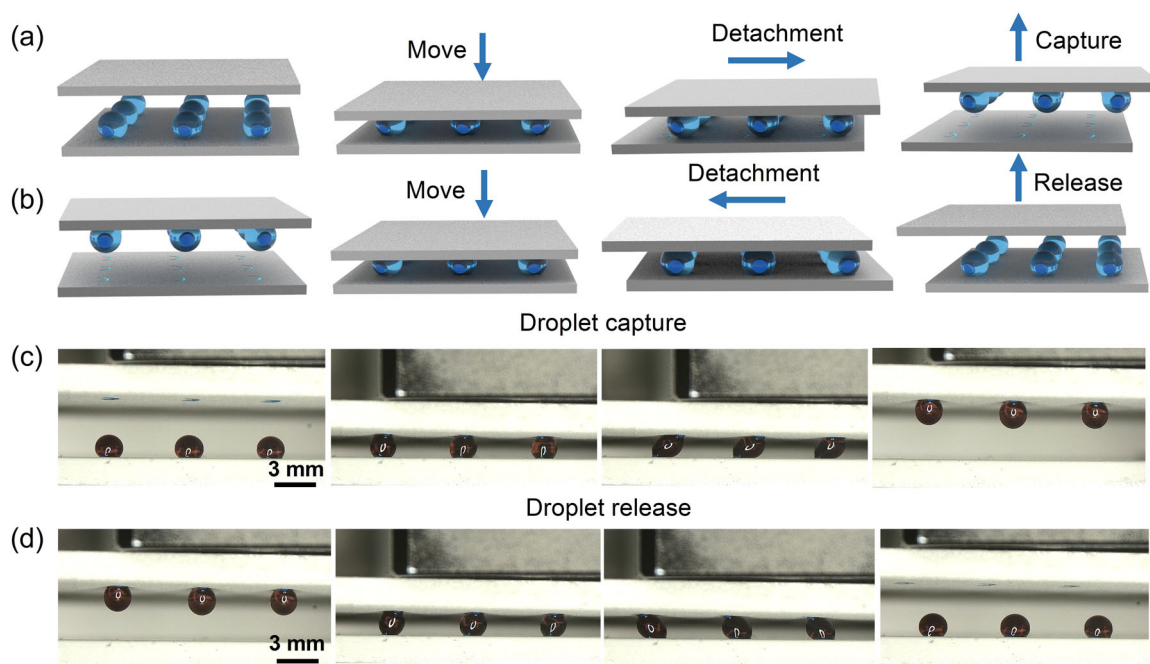


FIGURE 5 Droplet transfer without mass loss: (a, b) schematic and (c, d) experimental optical images of capturing and in situ releasing multiple droplets by using two face-to-face semicircular slippery lubricant-infused porous surface-patterned surfaces. Five microliters dyed DI water droplets were used in the experiment.

be implemented for multiple cycles without mass loss and is suitable for automated production with the aid of linear motors.

The above results show that a superamphiphobic surface patched with the SLIPS pattern enables excellent sliding anisotropy of a deposited droplet, which could be used to implement droplet manipulations precisely. Recently, the basic understanding of droplet interfacial phenomenon prompted some cutting-edge applications in the droplet-based microelectromechanical system (MEMS), such as droplet-based generators,¹¹ droplet-based self-driven mini boats,^{70,71} and liquid ring thrust bearing.⁷² Different from the discrete control of a single droplet intended for the droplet manipulation platform, the droplet-based MEMS systems typically require the continuous governing of droplet motion using arrayed patterned surfaces.⁷¹ In particular, the droplet friction property of the surface is crucial for energy transmission, determining the energy utilization or consumption rate. Therefore, in this section, we quantitatively characterize the tribological properties of droplets on the SLIPS array patterned surfaces to acquire the basic rules of the friction control of droplet-based MEMS parts, such as the droplet-based mini clutch. To achieve continuous governing of droplet friction, three SLIPS array patterned surfaces were designed based on the SLIPS patterns optimized in the above sections (Supporting Information: Figure S7). Dynamic droplet friction curves on the designed SLIPS array patterned surface in two opposite directions were obtained with a home-made microforce sensor with a measurement range of >1.00 N and a resolution of 0.02 μ N (Figure 6a and Supporting Information: Figure S8).⁷³ The dynamic sliding in the two directions was recorded by a CCD camera. The videos showed that the maximum deformation degree of the droplet in the D_{in} direction was much larger than that in the D_{out}

direction, indicating obvious droplet friction anisotropy (Supporting Information: Movie S3).

Droplet friction follows similar rules to sliding resistance. Semicircular SLIPS array patterned surfaces demonstrated the most significant droplet friction anisotropy with the outward (D_{out}) friction coefficient being 0.23–0.35, and the inward (D_{in}) being 0.55–0.70. A peak value of the friction coefficient appeared intermittently for both directions due to the given interval of the pattern array (Figure 6b). Regarding the sliding on the arrow-shaped SLIPS array patterned surface and horn-shaped SLIPS array patterned surface, the friction coefficients in the outward direction (D_{out}) were roughly the same as that regarding the semicircular SLIPS array patterned surface, while in the D_{in} direction, these two surfaces showed a much lower friction coefficient with the arrow-shaped one having 0.35–0.58 (Figure 6c) and the horn-shaped being 0.35–0.5 (Figure 6d). Obviously, the rules of steering the droplet friction coefficient of these SLIPS array patterned surfaces were just the same as the controlling of sliding resistance on SLIPS patterned surfaces, which further validates the reliability of the force analysis and the pattern design for droplet friction steering. It should be noted that the interval of the SLIPS pattern array may have an effect on the droplet friction steering. As the interval decreases, the number of the SLIPS patterns within the footprint of the fixed volume of a droplet increases. Thus, the droplet friction in the inward and outward directions and the friction differences in the two directions will be enhanced. The fluctuation of the droplet friction due to the discontinuous pattern layout may also be weakened. We believe that these patterned surfaces with a nearly twofold difference in

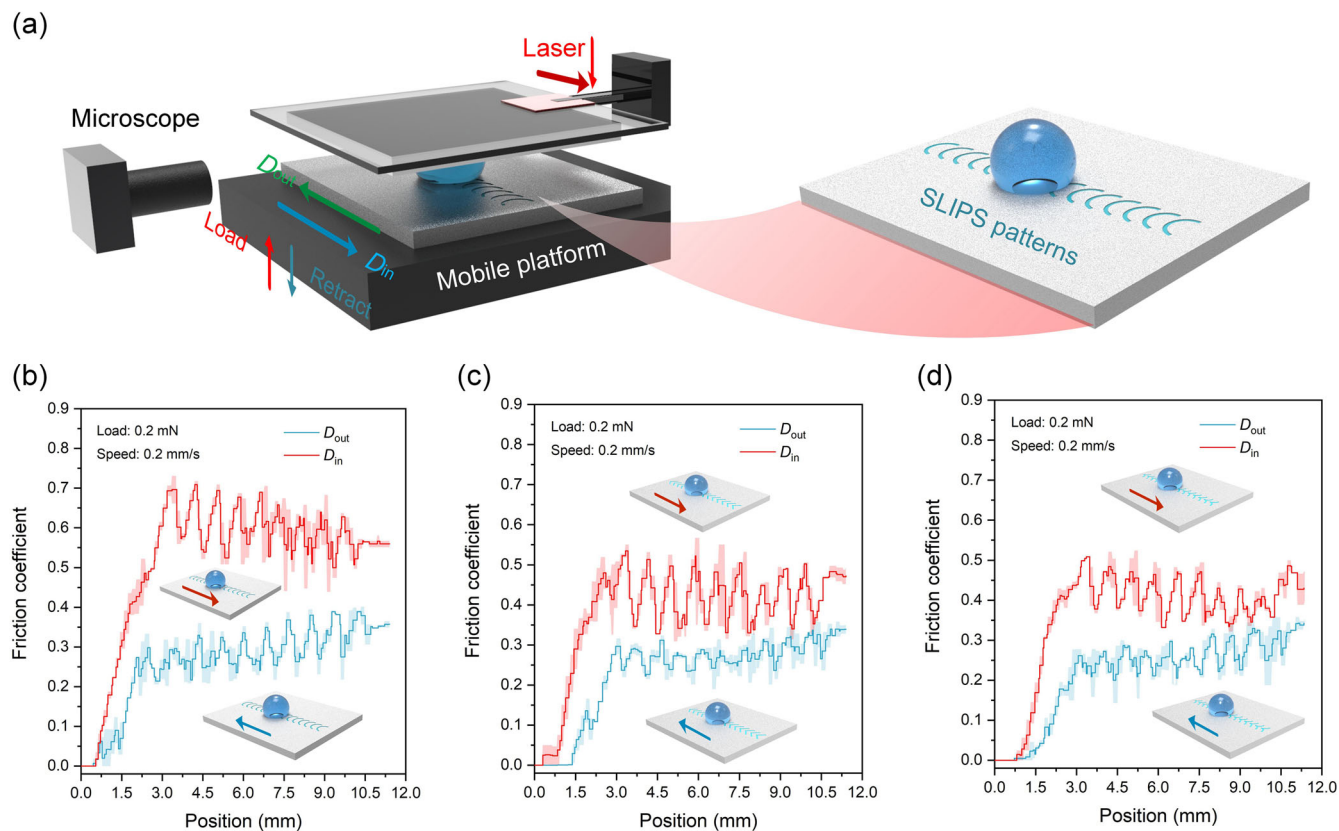


FIGURE 6 Steering of droplet friction: (a) schematic of apparatus for measuring the droplet friction on slippery lubricant-infused porous surface (SLIPS) array patterned surfaces; friction coefficient of a 25 μl droplet on surfaces patterned by (b) semicircular SLIPS array, (c) arrow-shaped SLIPS array, and (d) horn-shaped SLIPS array. The light back colors behind the curves in (b–d) represent the standard deviation of the data.

droplet friction in two opposite directions will enable the creation of the diode structure that serves as the droplet-based mini part to transfer and transmit the energy for various applications in microscales.

CONCLUSIONS

In summary, multi-bioinspired SLIPS patterned surfaces that allow for directional droplet sliding and precisely steering of droplet friction were created by coordinating the heterogeneous wettability of the back of the desert beetle, directional-dependent architecture of the butterfly wing, and ultraslippery configuration of the *N. alata*. Analysis of sliding resistance on typical SLIPS patterned surfaces revealed that the directional-dependent TPL immigration on the SLIPS patterns dominated the sliding anisotropy, which can be precisely predicted using the Fumidge equation. The sliding anisotropy is particularly strong for semicircular SLIPS patterns due to the most significant difference in TPL immigration in two opposite directions. By taking the advantage of the sliding anisotropy of the semicircular SLIPS patterned surfaces, sophisticated manipulation of multiple micro-liter-sized droplets without mass loss can be achieved via simple linear movement of the surface. This linear movement-triggered manipulation of the droplet array is easy to program and is crucial for high-throughput bioassays, which generally necessitate

the simultaneous handling of multiple droplets. In addition to the discrete control of droplets sliding off a single pattern intended for droplet manipulation, the continuous governing of droplet friction was enabled by designing the array of SLIPS patterns. The rules of the steering droplet friction coefficient of these SLIPS array patterned surfaces were just the same as the controlling of sliding resistance of the SLIPS patterned surface, which further validates the reliability of the force analysis and the pattern design for droplet friction steering.

A simple method involving electrochemical etching, chemical vapor deposition of a fluorinated silane, laser ablation, and lubricant infusing was proposed for scaled-up fabrication of such functional surfaces on different metallic substrates in real-world applications. We envision a potentially important use case to be controlled steering of droplet friction in space where surface tension-driven structures were allowed in the zero-gravity condition, enabling applications such as lab-on-a-chip devices and droplet-based microsystems for energy management.

MATERIALS AND METHODS

The aluminum sheets (70 mm \times 25 mm \times 2 mm) and copper sheets (70 mm \times 25 mm \times 2 mm) were purchased from Suzhou Metal Material Manufacturer. 1H,1H,2H,2H-Perfluorodecyltrimethoxysilane [$\text{CF}_3(\text{CF}_2)_7\text{CH}_2\text{CH}_2\text{Si}(\text{OCH}_3)_3$], lauric acid, hexadecane, and toluene were

purchased from Aladdin. All chemicals were analytically pure and were used as received.

The aluminum sheets (70 mm × 25 mm × 2 mm) were polished using sandpapers with three grades ($F = 400, 800, \text{ and } 1000$) to remove the excess oxidation layer, and then, the surface was subjected to the electrochemical etching process in 0.1 mol/L NaCl aqueous solution at a current density of 500 mA/cm² for 7 min to create irregular micron-sized rough structures. The etched aluminum sheets were subsequently soaked in boiling water for 40 min to form dense nanovillus overlaid on the microstructures. The treated samples were finally placed in a sealed chamber containing 0.3 g of toluene and 0.03 g of CF₃(CF₂)₇CH₂CH₂Si(OCH₃)₃ at 80°C for 3 h to obtain superamphiphobicity (CVD of the saline layer).

Superhydrophilic patterns were first fabricated on the prepared superamphiphobic surfaces using a UV laser micromachining system (KY-M-UV3L; Wuhan Keyi). The laser power of 2 W and the scanning speed of 10,000 mm/s were held constant during the process. SLIPS patterns were obtained by infusing 1 wt% hexadecane solution with lauric acid on the superhydrophilic patterns.

An SEM (SU8820) was used to analyze the micromorphology of prepared surfaces. The elements of the surfaces were characterized with EDS (Ultim Max). A goniometer (Rame-Hart 290) was used to measure static contact angles and sliding angles. A digital camera with a 1000 fps high-speed recording function (RX100M5; Sony) was used to record videos and images of droplet movement.

The droplet friction was tested on a home-made microforce sensor with a measurement range of >1.0 N and resolution of 0.02 μN. Detailed information about the test platform can be found in previous work.⁷³ A superhydrophobic aluminum sheet with a circular superhydrophilic pattern (diameter 3 mm) was fixed upside down on a glass substrate, which was installed at the end of two cantilever beams in horizontal and vertical directions. The force of the droplet in the horizontal and vertical directions can be obtained by measuring the deformation degree of the cantilever beam with a laser. The tested surface (SLIPS array patterned surface) was fixed on an XYZ-axial mobile platform, facing the circular superhydrophilic pattern located in the upper site. A 25 μl droplet was placed on the tested surface, and the mobile platform moved upward at a constant speed of 100 μm/s until the droplet touched the superhydrophilic pattern and was loaded with 0.2 mN. After loading, the mobile platform first moved in the D_{out} direction at a constant speed of 200 μm/s to measure the dynamic droplet friction and then implement the opposite moving to measure the friction in the D_{in} direction.

ACKNOWLEDGMENTS

This research was financially supported by the National Natural Science Foundation of China (51905267), the Natural Science Foundation of Jiangsu Province (BK20190411), the China Postdoctoral Science Foundation (2020TQ0148 and 2021M700072), the Fundamental Research Funds for the Central Universities (NT2020011), and the opening foundation of Aero-engine Thermal Environment and Structure Key Laboratory of Ministry of Industry and Information Technology of China (CEPE2020008).

CONFLICT OF INTEREST STATEMENT

The authors declare no conflict of interest.

ORCID

Biao Qi  <https://orcid.org/0000-0001-8708-7388>

Yao Lu  <http://orcid.org/0000-0001-9566-4122>

REFERENCES

- Li C, Yu C, Hao D, Wu L, Dong Z, Jiang L. Smart liquid transport on dual biomimetic surface via temperature fluctuation control. *Adv Funct Mater.* 2018;28:1707490.
- Huang G, Li M, Yang Q, et al. Magnetically actuated droplet manipulation and its potential biomedical applications. *ACS Appl Mater Interfaces.* 2017;9:1155-1166.
- Sun AC, Steyer DJ, Allen AR, Payne EM, Kennedy RT, Stephenson CRJ. A droplet microfluidic platform for high-throughput photochemical reaction discovery. *Nat Commun.* 2020;11:6202.
- Payne EM, Holland-Moritz DA, Sun S, Kennedy RT. High-throughput screening by droplet microfluidics: perspective into key challenges and future prospects. *Lab Chip.* 2020;20:2247-2262.
- Yao J, Yan Q, Qian Q, et al. Directional droplet transfer on micropillar-textured superhydrophobic surfaces fabricated using a ps laser. *Appl Surf Sci.* 2022;594:153414.
- Feng S, Zhu P, Zheng H, et al. Three-dimensional capillary ratchet-induced liquid directional steering. *Science.* 2021;373:1344-1348.
- Leng X, Sun L, Long Y, Lu Y. Bioinspired superwetting materials for water manipulation. *Droplet.* 2022;1:139-169.
- Qiao S, Li S, Li Q, Li B, Liu K, Feng X-Q. Friction of droplets sliding on microstructured superhydrophobic surfaces. *Langmuir.* 2017;33:13480-13489.
- Backholm M, Molpeceres D, Vuckovac M, et al. Water droplet friction and rolling dynamics on superhydrophobic surfaces. *Communications Materials.* 2020;1:64.
- Lv H, Yang Z, Liu B, et al. A flexible electromagnetic wave-electricity harvester. *Nat Commun.* 2021;12:834.
- Xu W, Zheng H, Liu Y, et al. A droplet-based electricity generator with high instantaneous power density. *Nature.* 2020;578:392-396.
- Li H, Fang W, Li Y, et al. Spontaneous droplets gyrating via asymmetric self-splitting on heterogeneous surfaces. *Nat Commun.* 2019;10:950.
- Chen H, Ran T, Gan Y, et al. Ultrafast water harvesting and transport in hierarchical microchannels. *Nat Mater.* 2018;17:935-942.
- Park K-C, Kim P, Grinthal A, et al. Condensation on slippery asymmetric bumps. *Nature.* 2016;531:78-82.
- Feng L, Zhang Y, Xi J, et al. Petal effect: a superhydrophobic state with high adhesive force. *Langmuir.* 2008;24:4114-4119.
- Wu D, Wu S-Z, Chen Q-D, et al. Curvature-driven reversible in situ switching between pinned and roll-down superhydrophobic states for water droplet transportation. *Adv Mater.* 2011;23:545-549.
- Lv J, Liu Y, Wei J, Chen E, Qin L, Yu Y. Photocontrol of fluid slugs in liquid crystal polymer microactuators. *Nature.* 2016;537:179-184.
- Gao F, Yao Y, Wang W, et al. Light-driven transformation of bio-inspired superhydrophobic structure via reconfigurable PAzoMA microarrays: from lotus leaf to rice leaf. *Macromolecules.* 2018;51:2742-2749.
- Wang Q, Xu B, Hao Q, Wang D, Liu H, Jiang L. In situ reversible underwater superwetting transition by electrochemical atomic alternation. *Nat Commun.* 2019;10:1212.
- Yang X, Li Y, Zheng H, Lu Y. Saturated surface charging on micro/nanoporous polytetrafluoroethylene for droplet manipulation. *ACS Appl Nano Mater.* 2022;5:3342-3351.
- Ge P, Zhang J, Liu Y, et al. Smart anisotropic wetting surfaces with reversed pH-responsive wetting directions. *Adv Funct Mater.* 2018;28:1802001.

22. Shu C, Su Q, Li M, Wang Z, Yin S, Huang S. Fabrication of extreme wettability surface for controllable droplet manipulation over a wide temperature range. *Int J Extrem Manuf.* 2022;4:045103.
23. Lin Y, Hu Z, Zhang M, et al. Magnetically induced low adhesive direction of nano/micropillar arrays for microdroplet transport. *Adv Funct Mater.* 2018;28:1800163.
24. Wu D, Wang J-N, Wu S-Z, et al. Three-level biomimetic rice-leaf surfaces with controllable anisotropic sliding. *Adv Funct Mater.* 2011;21:2927-2932.
25. Zheng Y, Gao X, Jiang L. Directional adhesion of superhydrophobic butterfly wings. *Soft Matter.* 2007;3:178-182.
26. Liu C, Ju J, Zheng Y, Jiang L. Asymmetric ratchet effect for directional transport of fog drops on static and dynamic butterfly wings. *ACS Nano.* 2014;8:1321-1329.
27. Li J, Zhou X, Li J, et al. Topological liquid diode. *Sci Adv.* 2017;3:eaa03530.
28. Feng S, Delannoy J, Malod A, Zheng H, Quéré D, Wang Z. Tip-induced flipping of droplets on Janus pillars: from local reconfiguration to global transport. *Sci Adv.* 2020;6:eabb4540.
29. Geng H, Bai H, Fan Y, et al. Unidirectional water delivery on a superhydrophilic surface with two-dimensional asymmetrical wettability barriers. *Mater Horiz.* 2018;5:303-308.
30. Tang Y, Yang X, Li Y, Zhu D. Design of hybrid superwetting surfaces with self-driven droplet transport feature for enhanced condensation. *Adv Mater Interfaces.* 2021;8:2100284.
31. Ghosh A, Ganguly R, Schutzius TM, Megaridis CM. Wettability patterning for high-rate, pumpless fluid transport on open, non-planar microfluidic platforms. *Lab Chip.* 2014;14:1538-1550.
32. Xu C, Feng R, Song F, et al. Continuous and controlled directional water transportation on a hydrophobic/superhydrophobic patterned surface. *Chem Eng J.* 2018;352:722-729.
33. Zhang L, Chen KS, Yu H-Z. Superhydrophobic glass microfiber filter as background-free substrate for quantitative fluorometric assays. *ACS Appl Mater Interfaces.* 2020;12:7665-7672.
34. Balu B, Berry AD, Patel KT, Breedveld V, Hess DW. Directional mobility and adhesion of water drops on patterned superhydrophobic surfaces. *J Adhes Sci Technol.* 2011;25:627-642.
35. Yang H, Sun K, Xue Y, et al. Controllable drop splashing on picosecond laser patterned hybrid superhydrophobic/-philic surfaces. *Appl Surf Sci.* 2019;481:184-191.
36. Feldmann D, Pinchasik B-E. How droplets move on surfaces with directional chemical heterogeneities. *J Phys Chem Lett.* 2021;12:11703-11709.
37. Yang X, Zhuang K, Lu Y, Wang X. Creation of topological ultraslippery surfaces for droplet motion control. *ACS Nano.* 2021;15:2589-2599.
38. Wei C, Zhang G, Zhang Q, Zhan X, Chen F. Silicone oil-infused slippery surfaces based on sol-gel process-induced nanocomposite coatings: a facile approach to highly stable bioinspired surface for biofouling resistance. *ACS Appl Mater Interfaces.* 2016;8:34810-34819.
39. Wong T-S, Kang SH, Tang SKY, et al. Bioinspired self-repairing slippery surfaces with pressure-stable omniphobicity. *Nature.* 2011;477:443-447.
40. Stamatopoulos C, Hemrle J, Wang D, Poulikakos D. Exceptional anti-icing performance of self-impregnating slippery surfaces. *ACS Appl Mater Interfaces.* 2017;9:10233-10242.
41. Zhuang K, Lu Y, Wang X, Yang X. Architecture-driven fast droplet transport without mass loss. *Langmuir.* 2021;37:12519-12528.
42. Luo H, Yin S, Huang S, Chen F, Tang Q, Li X. Fabrication of slippery Zn surface with improved water-impellent, condensation and anti-icing properties. *Appl Surf Sci.* 2019;470:1139-1147.
43. Li H, Aili A, Alhosani MH, Ge Q, Zhang T. Directional passive transport of microdroplets in oil-infused diverging channels for effective condensate removal. *ACS Appl Mater Interfaces.* 2018;10:20910-20919.
44. Chen F, Wang Y, Tian Y, et al. Robust and durable liquid-repellent surfaces. *Chem Soc Rev.* 2022;51:8476-8583.
45. Sharma M, Gupta S, Bhatt B, Bhatt G, Bhattacharya S, Khare K. Anisotropic motion of aqueous drops on lubricated chemically heterogeneous slippery surfaces. *Adv Mater Interfaces.* 2021;8:2001916.
46. You I, Lee TG, Nam YS, Lee H. Fabrication of a micro-omnifluidic device by omniphilic/omniphobic patterning on nanostructured surfaces. *ACS Nano.* 2014;8:9016-9024.
47. Qi B, Yang X, Wang X. Ultraslippery/hydrophilic patterned surfaces for efficient fog harvest. *Colloids Surf A.* 2022;640:128398.
48. Liu W, Pan R, Cai M, et al. Oil-triggered switchable wettability on patterned alternating air/lubricant-infused superamphiphobic surfaces. *J Mater Chem A.* 2020;8:6647-6660.
49. Liu W, Luo X, Chen C, et al. Directional anchoring patterned liquid-infused superamphiphobic surfaces for high-throughput droplet manipulation. *Lab Chip.* 2021;21:1373-1384.
50. Parker AR, Lawrence CR. Water capture by a desert beetle. *Nature.* 2001;414:33-34.
51. Yang X, Liu X, Lu Y, et al. Controlling the adhesion of superhydrophobic surfaces using electrolyte jet machining techniques. *Sci Rep.* 2016;6:23985.
52. Li J, Li J, Sun J, Feng S, Wang Z. Biological and engineered topological droplet rectifiers. *Adv Mater.* 2019;31:1806501.
53. Lu Y, Song J, Liu X, et al. Preparation of superoleophobic and superhydrophobic titanium surfaces via an environmentally friendly electrochemical etching method. *ACS Sustain Chem Eng.* 2013;1:102-109.
54. Song J, Huang S, Hu K, Lu Y, Liu X, Xu W. Fabrication of superoleophobic surfaces on Al substrates. *J Mater Chem A.* 2013;1:14783-14789.
55. Može M, Senegačnik M, Gregorčič P, Hočevar M, Zupančič M, Golobič I. Laser-engineered microcavity surfaces with a nanoscale superhydrophobic coating for extreme boiling performance. *ACS Appl Mater Interfaces.* 2020;12:24419-24431.
56. Zhao G, Xia H, Zhang Y, Li L, He N, Hansen HN. Laser-induced oxidation assisted micro milling of high aspect ratio microgroove on WC-Co cemented carbide. *Chin J Aeronaut.* 2021;34:465-475.
57. He H, Wang C, Zhang X, Ning X, Sun L. Facile fabrication of multi-scale microgroove textures on Ti-based surface by coupling the re-solidification bulges derived from nanosecond laser irradiation. *Surf Coat Technol.* 2020;386:125460.
58. Wang S, Feng L, Liu H, et al. Manipulation of surface wettability between superhydrophobicity and superhydrophilicity on copper films. *Chemphyschem.* 2005;6:1475-1478.
59. Balu B, Berry AD, Hess DW, Breedveld V. Patterning of superhydrophobic paper to control the mobility of micro-liter drops for two-dimensional lab-on-paper applications. *Lab Chip.* 2009;9:3066-3075.
60. Furmidge CGL. Studies at phase interfaces. I. The sliding of liquid drops on solid surfaces and a theory for spray retention. *J Colloid Sci.* 1962;17:309-324.
61. Olsen DA, Joyner PA, Olson MD. The sliding of liquid drops on solid surfaces. *J Phys Chem.* 1962;66:883-886.
62. Yang X, Choi WT, Liu J, Liu X. Droplet mechanical hand based on anisotropic water adhesion of hydrophobic-superhydrophobic patterned surfaces. *Langmuir.* 2019;35:935-942.
63. Sun G, Fang Y, Cong Q, Ren L. Anisotropism of the non-smooth surface of butterfly wing. *J Bionic Eng.* 2009;6:71-76.
64. Cai Z, Chen F, Tian Y, Zhang D, Lian Z, Cao M. Programmable droplet transport on multi-bioinspired slippery surface with tridirectionally anisotropic wettability. *Chem Eng J.* 2022;449:137831.

65. Küster SK, Pabst M, Jefimovs K, Zenobi R, Dittrich PS. High-resolution droplet-based fractionation of nano-LC separations onto microarrays for MALDI-MS analysis. *Anal Chem*. 2014;86:4848-4855.
66. Küster SK, Pabst M, Zenobi R, Dittrich PS. Screening for protein phosphorylation using nanoscale reactions on microdroplet arrays. *Angew Chem Int Ed*. 2015;54:1671-1675.
67. Wang Z, Yuan L, Wang L, Wu T. Stretchable superlyophobic surfaces for nearly-lossless droplet transfer. *Sens Actuators B*. 2017;244:649-654.
68. Tang X, Zhu P, Tian Y, Zhou X, Kong T, Wang L. Mechano-regulated surface for manipulating liquid droplets. *Nat Commun*. 2017;8:14831.
69. Sun Q, Wang D, Li Y, et al. Surface charge printing for programmed droplet transport. *Nat Mater*. 2019;18:936-941.
70. Song J, Guan F, Pan W, et al. Droplet-based self-propelled miniboat. *Adv Funct Mater*. 2020;30:1910778.
71. Chen Y, Yan D, Liu R, et al. Green self-propelling swimmer driven by rain droplets. *Nano Energy*. 2022;101:107543.
72. Wen J, Dini D, Reddyhoff T. Design and optimization of a liquid ring thrust bearing. *Tribol Int*. 2020;149:105588.
73. Li M, Huang W, Wang X. Advanced adhesion and friction measurement system. *Meas Sci Technol*. 2017;28:035601.

SUPPORTING INFORMATION

Additional supporting information can be found online in the Supporting Information section at the end of this article.

How to cite this article: Yang X, Qi B, Lu Y, Zhang W, Wang X. Bionic surface diode for droplet steering. *Droplet*. 2023;e46. doi:10.1002/dro2.46